

Unveiling the nuclear matter EoS from neutron star properties: a supervised machine learning approach

Márcio Ferreira^{1,*} and Constança Providência^{1,†}

¹*CFisUC, Department of Physics, University of Coimbra, P-3004 - 516 Coimbra, Portugal*

(Dated: October 15, 2019)

We explore supervised machine learning methods in extracting the non-linear maps between neutron stars (NS) observables and the equation of state (EoS) of nuclear matter. Using a Taylor expansion around saturation density, we have generated a model independent EoS set describing stellar matter constrained by nuclear matter parameters that are thermodynamically consistent, causal, and consistent with astrophysical observations. From this set, the full non-linear dependencies of the NS tidal deformability and radius on the nuclear matter parameters were learned using two distinct machine learning methods. Due to the high accuracy of the learned non-linear maps, we were able to analyze the impact of each nuclear matter parameter on the NS observables, identify dependencies on the EoS properties beyond linear correlations and predict which stars allow us to draw strong constraints.

I. INTRODUCTION

The properties of the equation of state (EoS) of nuclear matter at supra-saturation densities still remain an open question in nuclear physics. Neutron stars (NSs) become unique astrophysical objects through which the properties of super-dense neutron-rich nuclear matters can be studied. Constraining the EoS is then a combined task between astrophysics and nuclear physics. Astrophysical observables become then important probes for the dense nuclear matter properties. In particular, two-solar mass NS detected during the last tens years set quite stringent constraints on EoS of nuclear matter. The pulsar PSR J1614-2230 is among the most massive observed pulsars the one with the smallest uncertainty on the mass $M = 1.906 \pm 0.016 M_\odot$ [1–3]. Other two pulsars with a mass above two solar masses are PSR J0348+0432 with $M = 2.01 \pm 0.04 M_\odot$ [4] and the recently detected MSP J0740+6620 with a mass $2.14^{+0.10}_{-0.09} M_\odot$ [5], both masses given within a 68.3% credibility interval.

The coalescence of binary NS systems is a promising source of gravitational waves (GWs) [6–10]. The energy emitted in GW crucially depends on the EoS of NS matter, allowing to constraint the nuclear matter EoS from GW observations. One crucial information carried by GW is the tidal deformability of the NS [11, 12]. During the last inspiral stage of a coalescing binary NS system, each NS develops a mass-quadrupole moment due to the extremely strong tidal gravitational field of the companion NS. The ratio of the induced quadrupole moment to the external tidal field is proportional to the tidal deformability Λ . It an important observable that is sensitive to the nature of the EoS.

The compact binary inspiral event GW170817 was the first binary NS inspiral observation at the LIGO and Virgo observatories [9]. Due to its potential to directly probe the physics of NSs, it was acknowledged as the beginning of a new era in the field of multi-messenger astronomy and nuclear physics. The analysis of GW170817 have placed upper bounds on the NSs combined dimensionless tidal deformability. Using a low-spin prior (consistent with the observed neutron star population), a combined dimensionless tidal deformability of the NS merger is $\bar{\Lambda} \leq 800$ with 90 % confidence. A reanalysis of GW170817 was made assuming the same equation of state and spins within the range observed in Galactic binary neutron stars. The tidal deformability of a 1.4 solar mass NS was estimated to be $70 < \Lambda_{1.4 M_\odot} < 580$ at the 90% level [10].

Correlation analysis between nuclear matter parameters and NS properties have been explored using several nuclear models [13–21]. These correlations studies show, however, a considerable model dependence. One possible model-independent way of accessing the properties of the EoS is by parameterizing the EoS of asymmetric nuclear matter as a Taylor expansion around the saturation density [20–22].

In the present work, we explore supervised machine learning framework to learn the non-linear maps between the EoS and NS observables (we focus on the tidal deformability and radii). These non-linear maps encode the full dependency of the NS observables on the EoS, allowing to measure the effect of each empirical parameter. Unlike correlation analysis, which are only sensitive to linear dependences, these non-linear maps encode all kinds of dependencies and interactions among the EoS parameters. The supervised machine learning methodology has already been applied to neutron star physics in [23], where a Deep Neural Network (DNN) was used as an efficient procedure for mapping from a finite set of mass-radius observational data onto the equation

* marcio.ferreira@uc.pt

† cp@fis.uc.pt

of state plane. The analysis was later extended by comparing the DNN predictions with the conventional approaches for the nuclear equation of state and on the tidal deformability bound [24].

The paper is organized as follows. In Sec. II, we briefly describe both supervised machine learning methods used in the present work. In Sec. III, we outline the EoS parametrization employed. The EoS generating processing and the final EoS dataset, used in the supervised learning, is summarized in Sec. IV. The learning procedure is described in Sec. V and the results are shown in Sec. VI. Finally the conclusions are drawn in Sec. VII.

II. SUPERVISED MACHINE LEARNING

Our goal is to explore machine learning methods to learn the non-linear maps between the EoS of the nuclear matter and astrophysical observables. We will apply two supervised machine learning methods to access these non-linear maps. Bellow, we give a very general and brief introduction to these methods (for a rigorous exposition see [25–27]).

A. Support Vector Machines Regression

Support Vector Machines (SVM) is a well-known supervised machine learning method for classification problems. It is a maximum-margin classifier: it searches for the hyperplane (decision boundary) that separates the classes and has the maximum possible margin. The SVM are easily extended to non-linear classifiers using Kernel functions. They are non-linear maps that transform a non-linearly separable input space into a higher dimensional space where a linear separation is possible. It might be impossible, however, to find a hyperplane that perfectly separates the classes using only the input features. Then, a further generalization that allows margin violations is introduced using slack variables (soft-margin classifiers). A balance between having the largest possible margin while limiting the margin violations is searched. Support Vector Machines Regression (SVM-R) is the application of the above maximum-margin idea of SVM on regression problems. SVM-R searches for the maximum margin (hypertube of width ϵ) that encloses the maximum number of points while limiting margin violations (for a ϵ -insensitive loss regression). The regression model is the hyperplane positioned right at the center of this hypertube.

B. Deep Neural Networks

Deep Neural Networks (DNN) are widely-used nonlinear models for supervised learning. A DNN consists of

hierarchical layers made of neurons (the basic unit). In Feed-forward DNN, the input vector enters the first layer (input layer) and then proceeds sequentially through the middle layers (hidden layers) up to the last layer (output layer). At each neuron, a vector of features $\mathbf{x} = (x_1, \dots, x_d)$ is transformed into a scalar output y by two basic transformations: a linear transformation, which weights the relative importance of its inputs, and a non-linear transformation (activation function). First, the linear transformation $\mathbf{z} = \mathbf{w} \cdot \mathbf{x} + b$ is computed, where $\mathbf{w} = (w_1, w_2, \dots, w_d)$ are the neuron weights (it receives d input features), and b is the neuron bias. Then, the linear transformation \mathbf{z} passes through the activation function $\sigma(\mathbf{z})$. Some common choices are the rectified linear function, $\sigma(x) = \max\{0, x\}$, and the hyperbolic tangent, $\sigma(x) = \tanh(x)$. The output of one layer enters as input in the next layer. This procedure is repeated until the output layer is reached. The output of a DNN is then a complex non-linear transformation of the inputs that depends on all neurons weights and biases that compose all layers. Training a DNN consists in minimizing a loss function by the gradient descent method in order to find the optimal weights and biases. Herein, we use as loss function the Mean Squared Error (MSE), $L(\mathbf{w}, \mathbf{b}) = (1/N) \sum_i (\hat{y}_i(\mathbf{w}, \mathbf{b}) - y_i)^2$, where y_i is the actual output and $\hat{y}_i(\mathbf{w}, \mathbf{b})$ is the DNN's prediction.

III. EQUATIONS OF STATE

We parametrize the equation of state (EoS) of nuclear matter from a Taylor expansion around the saturation density. This has been done frequently in the past, see for instance [13, 16, 28, 29], and also recently [21, 22]. The coefficients of the expansion are identified with empirical parameters that characterize nuclear matter. Expressing the EoS in this form will allow us to analyze the properties of neutron stars systematically by varying the empirical parameters continuously within their uncertainty range. In the present study we will consider the expansion up to third order on the density.

We start from the generic functional form for the energy per particle of homogeneous nuclear matter

$$\mathcal{E}(n_n, n_p) = e_{sat}(n) + e_{sym}(n)\delta^2 \quad (1)$$

where $n = n_n + n_p$ is the baryonic density and $\delta = (n_n - n_p)/n$ is the asymmetry. By Taylor expanding this energy functional around the saturation density n_0 up to third order, we get

$$e_{sat}(x) = E_{sat} + \frac{1}{2}K_{sat}x^2 + \frac{1}{6}Q_{sat}x^3 \quad (2)$$

$$e_{sym}(n) = E_{sym} + L_{sym}x + \frac{1}{2}K_{sym}x^2 + \frac{1}{6}Q_{sym}x^3 \quad (3)$$

where x is defined as $x = (n - n_0)/(3n_0)$.

The isoscalar empirical parameters are defined as successive density derivatives of $e_{sat}(n)$,

$$P_{IS}^{(k)} = (3n_{sat})^k \left. \frac{\partial^k e_{sat}}{\partial n^k} \right|_{\{\delta=0, n=n_0\}}, \quad (4)$$

whereas the isovector parameters measure density derivatives of $e_{sym}(n)$,

$$P_{IV}^{(k)} = (3n_{sat})^k \left. \frac{\partial^k e_{sym}}{\partial n^k} \right|_{\{\delta=0, n=n_0\}}. \quad (5)$$

The corresponding empirical parameters are then

$$\{E_{sat}, K_{sat}, Q_{sat}\} \rightarrow \{P_{IS}^{(0)}, P_{IS}^{(2)}, P_{IS}^{(3)}\} \quad (6)$$

and

$$\{E_{sym}, L_{sym}, K_{sym}, Q_{sym}\} \rightarrow \{P_{IV}^{(0)}, P_{IV}^{(1)}, P_{IV}^{(2)}, P_{IV}^{(3)}\}. \quad (7)$$

Each EoS is represented by a point in a 7-dimensional input space: $(E_{sat}, K_{sat}, Q_{sat}, E_{sym}, L_{sym}, K_{sym}, Q_{sym})$. The EoS are generated by sampling on this space. The probability of an EoS is given by a multivariate Gaussian distribution with diagonal covariance - we do not impose correlations on the empirical parameters a priori. The physical correlations among the empirical parameters arise from a set of physical constraints [30, 31]. A valid EoS must fulfill the following conditions: i) be monotonically increasing (thermodynamic stability); ii) the speed of sound must not exceed the speed of light (causality); iii) supports a maximum mass at least as high as $1.97M_\odot$ [1–4] (observational consistency); iv) predicts a tidal deformability of $70 < \Lambda_{1.4M_\odot} < 580$ [10] (observational consistency); and v) the symmetry energy $e_{sym}(n)$ is positive. All the EoS are in β -equilibrium. For the low density region we use the SLy4 EoS [32]. To be considered a valid EoS, the generated EoS must cross the SLy4 EoS in the $P(\mu)$ plane below n_0 .

We calculate both the mass-radius relation, by solving the Tolman-Oppenheimer-Volkoff [33, 34] equation, and the tidal deformability Λ [12].

IV. EOS DATASET

Being a rather well determined quantity and to reduce the computational cost, we have fixed the value of the saturation energy $E_{sat} = -15.8$ MeV (the current estimated value is -15.8 ± 0.3 MeV [30]). Furthermore, the saturation density is also fixed at $n_0 = 0.155 \text{ fm}^{-3}$. We have generated 10^8 EoS by sampling from the 6-dimensional EOS parameter space

$$\text{EoS}_i = (K_{sat}, Q_{sat}, E_{sym}, L_{sym}, K_{sym}, Q_{sym})_i \sim N(\boldsymbol{\mu}, \boldsymbol{\Sigma}),$$

where the mean vector components μ_i and covariance matrix entries σ_{ii} ($\sigma_{ij} = 0$, no correlation between the

	μ_i [MeV]	$\sqrt{\sigma_{ii}}$ [MeV]
K_{sat}	230	20
Q_{sat}	300	400
E_{sym}	32	2
L_{sym}	60	15
K_{sym}	-100	100
Q_{sym}	0	400

Table I. The mean and standard deviation $\sqrt{\sigma_{ii}}$ of the multivariate Gaussian, where σ_{ii} is the variance.

empirical parameters) are in Table I. The standard deviation $\sqrt{\sigma_{ii}}$ values reflect a global estimation for the empirical parameters [30].

After all the constraints have been applied to each sampled EoS, we ended up with a set of 13038 EoS. The sample mean and standard deviations for the empirical parameters for this final set are in Table II.

	μ_i [MeV]	$\sqrt{\sigma_{ii}}$ [MeV]
K_{sat}	232.92	18.37
Q_{sat}	-94.02	29.57
E_{sym}	33.20	1.83
L_{sym}	51.85	11.25
K_{sym}	-60.83	55.74
Q_{sym}	290.03	215.96

Table II. Sample mean $\mu_i = (1/N) \sum_i x_i$ and standard deviation $\sqrt{\sigma_{ii}} = \sqrt{\sum_i (x_i - \bar{x})^2 / (N - 1)}$ for the empirical parameters of the 13038 valid models

The obtained $M - R$ and $M - \Lambda$ diagrams, for the entire set of 13038 EoS, are shown in Fig. 1. The mean values of Λ_{M_i} and R_{M_i} and their standard deviations for $1.0M_\odot, 1.4M_\odot$ and $1.9M_\odot$ are in Table III.

	μ_i	$\sqrt{\sigma_{ii}}$
$\Lambda_{1.0M_\odot}$	2808.887	261.523
$\Lambda_{1.4M_\odot}$	415.723	46.179
$\Lambda_{1.9M_\odot}$	41.977	9.972
	μ_i [km]	$\sqrt{\sigma_{ii}}$ [km]
$R_{1.0M_\odot}$	11.950	0.190
$R_{1.4M_\odot}$	12.055	0.194
$R_{1.9M_\odot}$	11.713	0.317

Table III. Model predictions for Λ_{M_i} and R_{M_i}

The resulting distribution for the NS radius is quite narrower, e.g., for the canonical mass of $1.4M_\odot$ the dispersion is only of 0.19 km around the mean value of 12.05 km (Table III). For the same NS mass, the tidal deformability is centered around 417.72 with a dispersion of 46.18.

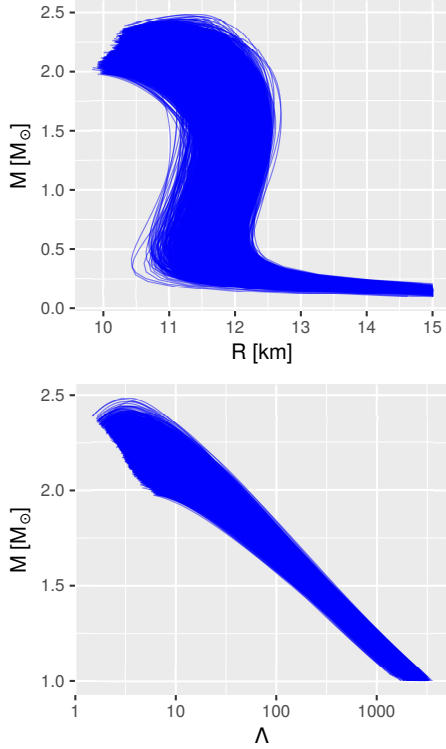


Figure 1. Mass-radius and mass- Λ relations for the set of 13038 EoS.

V. LEARNING PROCEDURE

Our goal is to use the Deep Neural Networks (DNN) and Support Vector Machines Regression (SVM-R) models to learn the non-linear maps between the equation of state, i.e., the empirical parameters of nuclear matter, and neutron stars observables. Herein, we focus on the neutron star radius and tidal deformability as a function of the neutron stars mass. Therefore, the non-linear maps one wants to learn are:

$$\Lambda_{M_i}(K_{sat}, Q_{sat}, E_{sym}, L_{sym}, K_{sym}, Q_{sym}), \quad (8)$$

$$R_{M_i}(K_{sat}, Q_{sat}, E_{sym}, L_{sym}, K_{sym}, Q_{sym}). \quad (9)$$

For the learning procedure, we have randomly splitted our data-set (13038 EoS) into two sets: training (80%) and test (20%). The models are trained on the training set and, once we select the model with higher performance, we determine its accuracy on the test set (the test set is only used once). For training, we have employed a 5-fold validation¹. All data were normalized. The evaluation metric used is the Mean Squared Error (MSE),

¹ This approach consists in splitting the train data into five partitions of equal size; then for each partition i , the model is trained on the remaining 4 partitions and evaluated on partition i . The final model accuracy is the average of the 5 accuracy values obtained.

$MSE = (1/N) \sum_i (\hat{y}_i - y_i)^2$, where \hat{y}_i is the model prediction, y_i is the true value, and N is the number of points.

The DNN were trained using the Keras library [35] with the TensorFlow backend [36]. For the optimization we employed the Adam algorithm [37] with a batch size of 32 with the MSE loss function. We used grid search to find the best DNN structure, i.e., the number of activation layers, the number of units per layer, and the activation functions. The best SVM-R model was also selected using a grid search, with the radial basis kernel function.

VI. RESULTS

After obtaining the best models by grid search, we determine their accuracy on the test set. This is the generalization capacity of the models, i.e., their predictability power on unseen data (data not used for training). The results are in Table IV.

\hat{y}	RMSE		(RMSE/ \bar{y}) \times 100%	
	DNN	SVM-R	DNN	SVM-R
$\Lambda_{1.0M_\odot}$	16.646	23.547	0.59	0.84
$\Lambda_{1.4M_\odot}$	1.932	2.236	0.46	0.54
$\Lambda_{1.9M_\odot}$	0.227	0.556	0.54	1.32
$R_{1.0M_\odot}$ [km]	0.007	0.012	0.06	0.10
$R_{1.4M_\odot}$ [km]	0.006	0.010	0.05	0.08
$R_{1.9M_\odot}$ [km]	0.007	0.019	0.06	0.16

Table IV. Root Mean Square Error (RMSE), $\sqrt{(1/N) \sum_i (\hat{y}_i - y_i)^2}$, for the Deep Neural Networks (DNN) and Support Vector Machines Regression (SVM-R) methods on the test set. We also show the normalized Root Mean Square Error, RMSE/ \bar{y} , expressed as a percentage.

DNN shows higher accuracies than SVM-R. To compare the models performance on different scales quantities, we show the normalized root mean square error (in percentage) in Table IV. The predictability power remains almost constant for both Λ_{M_i} and R_{M_i} . For the canonical neutron star $1.4M_\odot$, we have a prediction accuracy below 0.1% for $R_{1.4M_\odot}$ and 1% for $\Lambda_{1.4M_\odot}$ for both the DNN and SVM-R analysis. Therefore, from the EoS empirical parameters, we can infer both $\Lambda_{1.4M_\odot}$ and $R_{1.4M_\odot}$ with an average accuracy of $\Delta\Lambda = 1.932$ and $\Delta R = 0.006$ km using DNN, and $\Delta\Lambda = 2.236$ and $\Delta R = 0.010$ km using SVM-R.

Having successfully learned the non-linear functions between the feature space (empirical parameters) and the target space (neutron stars observables), one can now explore the concept of feature importance. It consists in measuring the impact of each empirical parameter (feature) on the Λ_{M_i} and R_{M_i} predictions. We analyze the prediction error (on the test set) after randomly

permuting the values of each empirical parameter separately. Then, if an empirical parameter is important for the non-linear mapping, shuffling its values increases the prediction error, i.e., the model prediction relies strongly on this empirical parameter. If, on the other hand, by shuffling the values of that empirical parameter the error remains almost unchanged, we can say that the empirical parameter has a smaller impact on the non-linear map. The increase on the RMSE for the DNN prediction is in Table V. The K_{sat} is shown to be the most important parameter in predicting both the R_M and Λ_M . K_{sym} and Q_{sym} show almost no impact on R for low neutron star masses but become important for heavier neutron stars. Q_{sym} is the second most important parameter in predicting both $R_{1.9M_\odot}$ and $\Lambda_{1.9M_\odot}$. Contrarily to the usual correlation analyses, which is only sensitive to linear dependences, we are accessing herein the impact of each feature on the non-linear map while controlling for the other parameters (we are isolating the impact of each parameter). The results for the SVM-R agree with DNN results at a level that is generally below 10%, i.e., the relative importance of each empirical parameter is almost the same. These results show that both methods are learning the same non-linear dependencies.

	$R_{1.0M_\odot}$	$R_{1.4M_\odot}$	$R_{1.9M_\odot}$	$\Lambda_{1.0M_\odot}$	$\Lambda_{1.4M_\odot}$	$\Lambda_{1.9M_\odot}$
	[km]	[km]	[km]			
K_{sat}	0.152	0.225	0.474	255.617	58.624	13.449
Q_{sat}	0.031	0.073	0.285	62.353	20.357	8.170
E_{sym}	0.059	0.030	0.014	46.970	7.396	0.831
L_{sym}	0.119	0.101	0.096	151.705	18.742	2.977
K_{sym}	0.126	0.146	0.259	177.651	34.723	6.491
Q_{sym}	0.077	0.139	0.414	124.981	31.226	9.151

Table V. Feature importance of the DNN predictions as measured by the increase on RMSE when the values of each empirical parameter are randomly shuffled.

The relevance of having successfully learned the non-linear maps between the empirical parameters and NS observables is that we are now able to study their dependencies. Considering the big uncertainty on the empirical parameters, we first analyze the impact of both Q_{sym} and Q_{sat} , which are two of the most uncertain empirical parameters, on Λ_{M_i} and R_{M_i} . To analyze $\Lambda_{M_i}(Q_{sym}, Q_{sat})$ and $R_{M_i}(Q_{sym}, Q_{sat})$, we have fixed: $K_{sat} = 233$ MeV, $E_{sym} = 33$ MeV, $L_{sym} = 52$ MeV within the range of values constrained by experiment. For K_{sym} we will consider $K_{sym} = \pm 61$ MeV taking into account our lack of knowledge on this quantity. The symmetry energy curvature has been constrained to the intervals $K_{sym} = -111.8 \pm 71.3$ MeV in [38], -112 MeV $< K_{sym} < -52$ MeV in [19], and -394 MeV $< K_{sym} < 168$ MeV in [20]. Figure 2 shows the $\Lambda_{1.4M_\odot}(Q_{sym}, Q_{sat})$ map for DNN (left), SVM-R (middle), and the difference between both predictions (right), taking $K_{sym} = 61$ MeV. Both

DNN and SVM-R show an almost linear dependence, i.e. $\Lambda_{1.4M_\odot} \sim aQ_{sym} + bQ_{sat}$. The same behavior is seen for $R_{1.4M_\odot}(Q_{sym}, Q_{sat})$. In fact, when we subtract their predictions (right) we see that the prediction discrepancy between both models is as low as 5.

We now consider take $K_{sym} = -61$, which lies inside all ranges defined in [19, 20, 38]. The SVM prediction for $\Lambda_{M_i}(Q_{sym}, Q_{sat})$ (top panels) and $R_{M_i}(Q_{sym}, Q_{sat})$ (bottom panels) are in Fig. 3, where M_i takes the following values: $1.0M_\odot$ (left), $1.4M_\odot$ (center), and $1.9M_\odot$ (right). Both R_{M_i} and Λ_{M_i} show a similar dependence as we consider more massive NS masses. Even though there is an almost linear dependence $\Lambda \sim aQ_{sym} + bQ_{sat}$ for both $1.0M_\odot$ and $1.4M_\odot$, the role played by Q_{sym} changes as it increases. There is a weak enhancement effect on Λ and R for $1.0M_\odot$ and $1.4M_\odot$ as Q_{sym} increases for a fixed Q_{sat} . A different pattern happens for $1.9M_\odot$ showing a non-linear dependency.

It is interesting to notice that when we compare the results for $\Lambda_{1.4M_\odot}$ while fixing $K_{sym} = 61$ MeV (middle panel of Fig 2) with $K_{sym} = -61$ MeV (top middle panel of Fig. 3), the dependence of $\Lambda_{1.4M_\odot}$ on Q_{sat} , Q_{sym} has changed: low Q_{sym} values enhances $\Lambda_{1.4M_\odot}$ for $K_{sym} = -61$ MeV and a fixed Q_{sat} , while it suppresses $\Lambda_{1.4M_\odot}$ for $K_{sym} = 61$ MeV.

We now analyze the dependencies of Λ_{M_i} and R_{M_i} on L_{sym} and K_{sat} , i.e., the non-linear functions $\Lambda_{M_i}(L_{sym}, K_{sat})$ and $R_{M_i}(L_{sym}, K_{sat})$, by fixing $Q_{sat} = -94$ MeV, $E_{sym} = 33$ MeV, $Q_{sym} = 290$ MeV, and $K_{sym} = -61$ MeV. The results for $\Lambda_{M_i}(L_{sym}, K_{sat})$ and $R_{M_i}(L_{sym}, K_{sat})$ are plotted in Fig. 4 and show a highly non-linear dependence. The first conclusion is the big effect of K_{sat} on Λ_{M_i} , confirming the result in Table V as the most important feature in explaining Λ_{M_i} . Furthermore, the weak dependence of both Λ_{M_i} and R_{M_i} on L_{sym} seen in Fig. 4 also supports its low impact (see Table V). The value of Λ_{M_i} is almost insensitive to the value of L_{sym} and it is a highly non-linear dependence. Increasing K_{sat} makes Λ_{M_i} and R_{M_i} bigger. The $R_{M_i}(L_{sym}, K_{sat})$ shows the similar trend as for $\Lambda_{M_i}(L_{sym}, K_{sat})$ but with highly non-linear dependencies. Let us stress that these results are just indicating that after $\{Q_{sat}, E_{sym}, Q_{sym}, K_{sym}\}$ have been fixed to the above values, both Λ_{M_i} and R_{M_i} are sensitive to K_{sat} and not to L_{sym} .

In [18] a linear correlation between the star radius and the linear combination $K_{sat} + \alpha L_{sym}$ was obtained within a set of 33 EoS determined from both RMF and Skrme energy functionals, constrained to nuclear properties. A strong correlation between this linear combination of EoS parameters and the tidal deformability was also discussed in [19]. However, in [20] within a larger set of models including the 33 EoS used in the above references and supplemented with extra 88 phenomenological EoSs, constructed by randomly sampling the nuclear parameters K_{sat} , Q_{sat} , E_{sym} , L_{sym} , and K_{sym} , a much weaker cor-

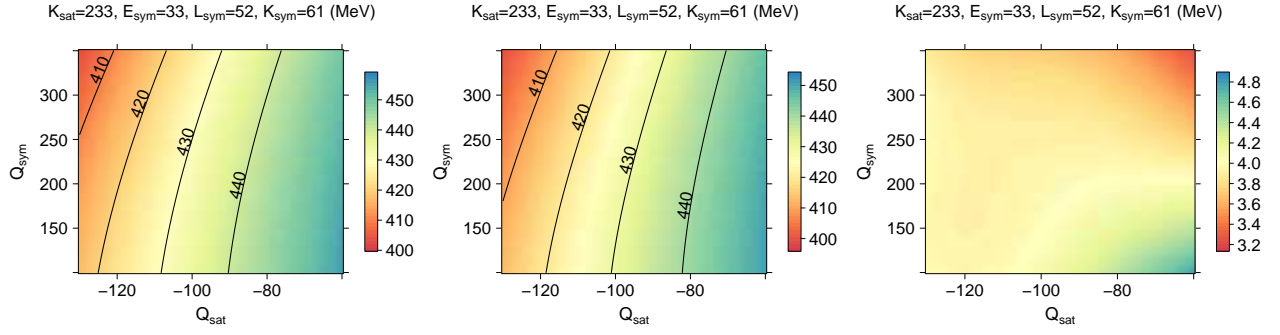


Figure 2. The DNN (left) and SVMR (center) predictions for $\Lambda_{1.4M_\odot}$ as a function of Q_{sym} and Q_{sat} fixing: $K_{sat} = 233$ MeV, $E_{sym} = 33$ MeV, $L_{sym} = 52$ MeV, and $K_{sym} = 61$ MeV. The difference between DNN and SVMR prediction is shown in the right panel.

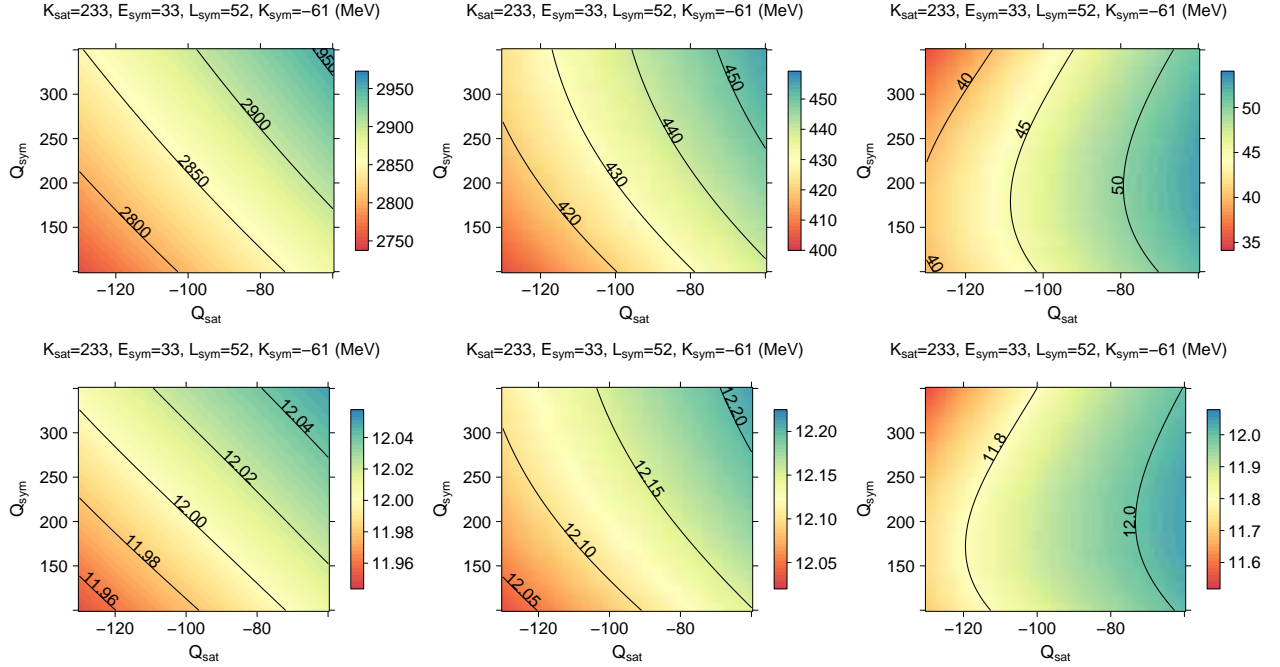


Figure 3. SVM-R predictions $\Lambda_{M_i}(Q_{sym}, Q_{sat})$ (top) and $R_{M_i}(Q_{sym}, Q_{sat})$ [km] (bottom) for $M_i = 1.0M_\odot$ (left), $M_i = 1.4M_\odot$ (center), $M_i = 1.9M_\odot$ (right), having fixed: $K_{sat} = 233$ MeV, $E_{sym} = 33$ MeV, $L_{sym} = 52$ MeV, and $K_{sym} = -61$ MeV.

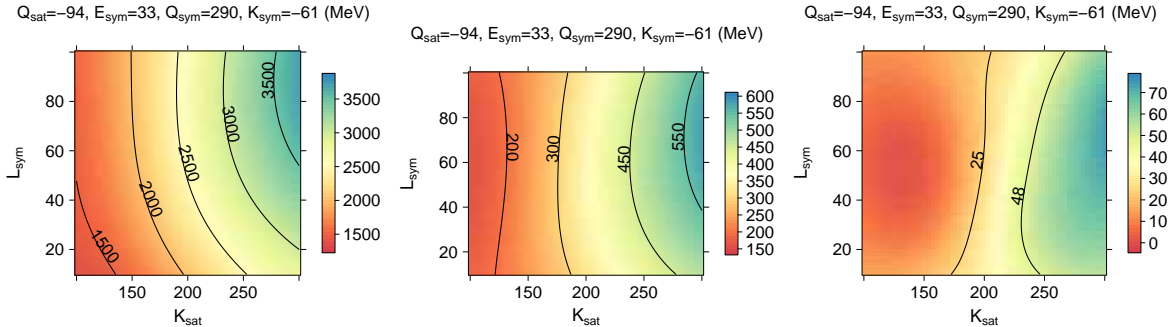


Figure 4. SVM-R predictions $\Lambda_{M_i}(L_{sym}, K_{sat})$ (top) and $R_{M_i}(L_{sym}, K_{sat})$ [km] (bottom) for $M_i = 1.0M_\odot$ (left), $M_i = 1.4M_\odot$ (center), $M_i = 1.9M_\odot$ (right), having fixed: $Q_{sat} = -94$ MeV, $E_{sym} = 33$ MeV, $Q_{sym} = 290$ MeV, and $K_{sym} = -61$ MeV.

relation with the tidal deformability was obtained. The difference is probably due to the fact the 33 EoS of stud-

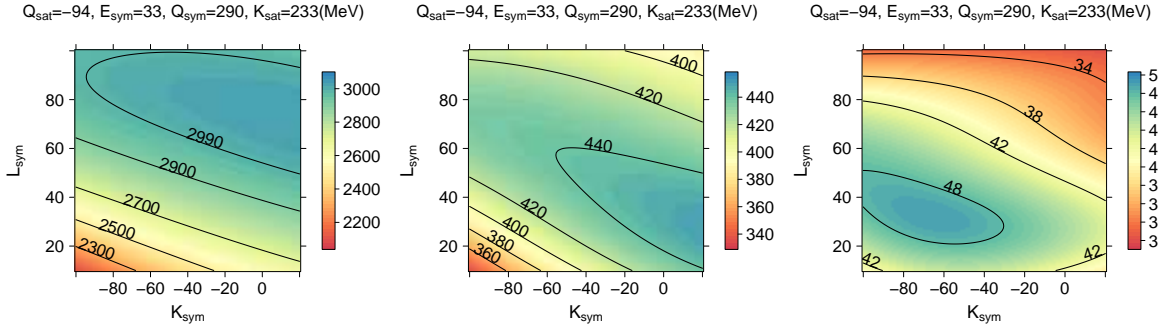


Figure 5. SVM-R predictions $\Lambda_{M_i}(L_{sym}, K_{sym})$ (top) and $R_{M_i}(L_{sym}, K_{sym})$ [km] (bottom) for $M_i = 1.0M_\odot$ (left), $M_i = 1.4M_\odot$ (center), $M_i = 1.9M_\odot$ (right), having fixed: $Q_{sat} = -94$ MeV, $E_{sym} = 33$ MeV, $Q_{sym} = 290$ MeV, and $K_{sat} = 233$ MeV.

ies [18, 19] include more constraints from nuclear matter properties than the 88 phenomenological EoS constructed from metamodels in [20].

In [20] a strong correlation was found between the average tidal deformability $\tilde{\Lambda}$ for all mass fractions compatible with the GW170817 and the linear combination $L_{sym} + \lambda K_{sym}$. In the following we analyze the dependencies of Λ_{M_i} and R_{M_i} on L_{sym} and K_{sym} , by fixing $Q_{sat} = -94$ MeV, $E_{sym} = 33$ MeV, $Q_{sym} = 290$ MeV, and $K_{sat} = 233$ MeV. The results are in Fig. 5. It is interesting to notice the existence of islands in the (L_{sym}, K_{sym}) space that gives the maximum values for Λ_{M_i} and R_{M_i} . Fixing $K_{sym} = -40$ MeV, for example, gives rise to a non-monotonic behavior in $\Lambda(L_{sym})$ and $R(L_{sym})$. However, for low values of L_{sym} and K_{sym} , there is an almost linear dependence in Λ_{M_i} and R_{M_i} for $M_i = 1.0M_\odot$ and $M_i = 1.4M_\odot$. The importance of having the non-linear maps between NS observables and the empirical parameters is clear when comparing Figures 4 and 5. The effect of a parameter, e.g., L_{sym} , is only measurable once the set of remaining parameters are fixed and, furthermore, it crucially depends on their values.

A correlation between the NS radii and K_{sym} is reported in [19], in particular if $M < 1.4M_\odot$. Moreover, K_{sym} and $K_{sym} + \gamma L_{sym}$ are seen to be strongly correlated with the tidal deformability for the star masses covered by GW170817 [20, 39]. Figure 5 reflects this fact: a linear dependence is found for $\Lambda_{1.0M_\odot}(L_{sym}, K_{sym})$ and $\Lambda_{1.4M_\odot}(L_{sym}, K_{sym})$ if one considers an EoS set characterized by $L_{sym} < 60$ MeV and $K_{sym} < -20$ MeV. Furthermore, Fig. 5 shows why the above correlations become weaker with increasing NS solar masses: their dependencies became essentially non-linear as M_i increases. The NS radius show similar dependencies. Universal relations between the NS observables and the nuclear parameters captured by correlation analysis rely on the linear leading-order behavior of these non-linear maps. As soon as the non-linear dependencies become important, correlation analysis can no longer be used to constraint the nuclear parameters.

VII. CONCLUSIONS

In the present work we have shown how supervised machine learning tools allow us to obtain NS properties, like the radius and tidal deformability, in terms of a set of seven parameters that characterizes the EoS of stellar matter. Two methods have been tested, Deep Neural Networks (DNN) and Support Vector Machines Regression (SVM-R), and although similar, DNN shows higher accuracies.

First a set of more than 10^4 EoS, for which the pressure is an increasing function of density and the symmetry energy is non-negative, and describing stellar matter constrained by nuclear matter properties, observations and causality, was generated. Machine learning methods were next applied using this set of models to learn the map between empirical parameters of the nuclear matter EoS and astrophysical observables. We have shown that a very large accuracy is attainable.

In order to test the properties of the non-linear map obtained between the EoS parameters and the NS radius R and tidal deformability Λ , we have studied in a two parameter plan X_i, X_j how R and Λ behave, considering all the other parameters fixed. In particular, we could show that the tidal deformability and the radius seem to be quite insensitive to the slope L_{sym} , except perhaps for the smaller stellar masses, but very sensitive to the incompressibility K_{sat} . We also show that the radius and tidal deformability are also sensitive to the curvature K_{sym} . Finally we have obtained a clear linear dependence of the tidal deformability on the linear combination $L_{sym} + \lambda K_{sym}$ for the masses $M \lesssim 1.4M_\odot$ if K_{sym} is small enough, otherwise a non-linear behavior is obtained which will destroy a possible correlation between $L_{sym} + \lambda K_{sym}$ and the tidal deformability. This drove us to the conclusion that if the non-linear dependencies become important, correlations analysis can no longer be used to constraint the nuclear parameters. A supervised machine learning approach allows us to go beyond linear correlations and identify under which conditions astrophysical observations of neutron stars constrain the EoS of dense nuclear matter. In fact, some nonlinear com-

bination of nuclear parameters neutron star properties have already been studied in past works [40, 41]. In the future the EoS dataset used as training set will be generalized to a wider domain of acceptable models, including models that predict a first order phase transition.

ACKNOWLEDGMENTS

This article is based upon work partially funded by COST Action CA17137 G2NET and COST Action

CA16214 PHAROS supported by COST (European Cooperation in Science and Technology), and by the FCT (Portugal) Projects No.UID/FIS/04564/2019 and POCI-01-0145-FEDER-029912.

-
- [1] Z. Arzoumanian *et al.* (NANOGrav), *Astrophys. J. Suppl.* **235**, 37 (2018), arXiv:1801.01837 [astro-ph.HE].
- [2] E. Fonseca *et al.*, *Astrophys. J.* **832**, 167 (2016), arXiv:1603.00545 [astro-ph.HE].
- [3] P. Demorest, T. Pennucci, S. Ransom, M. Roberts, and J. Hessels, *Nature* **467**, 1081 (2010), arXiv:1010.5788 [astro-ph.HE].
- [4] J. Antoniadis *et al.*, *Science* **340**, 6131 (2013), arXiv:1304.6875 [astro-ph.HE].
- [5] H. T. Cromartie *et al.*, (2019), 10.1038/s41550-019-0880-2, arXiv:1904.06759 [astro-ph.HE].
- [6] C. Cutler, T. A. Apostolatos, L. Bildsten, L. S. Finn, E. E. Flanagan, D. Kennefick, D. M. Markovic, A. Ori, E. Poisson, G. J. Sussman, and K. S. Thorne, *Phys. Rev. Lett.* **70**, 2984 (1993).
- [7] C. Cutler and K. S. Thorne, in *Proceedings, 16th International Conference on General Relativity and Gravitation*, KDunak, South, Africa, and July 15-19, 2001 (2013) pp. 72–111, arXiv:gr-qc/0204090 [gr-qc].
- [8] D. Radice, S. Bernuzzi, W. Del Pozzo, L. F. Roberts, and C. D. Ott, *Astrophys. J.* **842**, L10 (2017), arXiv:1612.06429 [astro-ph.HE].
- [9] B. P. Abbott *et al.* (LIGO Scientific, Virgo), *Phys. Rev. Lett.* **119**, 161101 (2017), arXiv:1710.05832 [gr-qc].
- [10] B. P. Abbott *et al.* (LIGO Scientific, Virgo), *Phys. Rev. Lett.* **121**, 161101 (2018), arXiv:1805.11581 [gr-qc].
- [11] É. É. Flanagan and T. Hinderer, *Phys. Rev. D* **77**, 021502 (2008), arXiv:0709.1915 [astro-ph].
- [12] T. Hinderer, *Astrophys. J.* **677**, 1216 (2008), arXiv:0711.2420 [astro-ph].
- [13] I. Vidana, C. Providencia, A. Polls, and A. Rios, *Phys. Rev. C* **80**, 045806 (2009), arXiv:0907.1165 [nucl-th].
- [14] J. Xu, L.-W. Chen, B.-A. Li, and H.-R. Ma, *Astrophys. J.* **697**, 1549 (2009), arXiv:0901.2309 [astro-ph.SR].
- [15] C. Ducoin, J. Margueron, and C. Providencia, *EPL* **91**, 32001 (2010), arXiv:1004.5197 [nucl-th].
- [16] C. Ducoin, J. Margueron, C. Providencia, and I. Vidana, *Phys. Rev. C* **83**, 045810 (2011), arXiv:1102.1283 [nucl-th].
- [17] W. G. Newton, M. Gearheart, and B.-A. Li, *Astrophys. J. Suppl.* **204**, 9 (2013), arXiv:1110.4043 [astro-ph.SR].
- [18] N. Alam, B. K. Agrawal, M. Fortin, H. Pais, C. Providência, A. R. Raduta, and A. Sulaksono, *Phys. Rev. C* **94**, 052801 (2016), arXiv:1610.06344 [nucl-th].
- [19] T. Malik, N. Alam, M. Fortin, C. Providência, B. K. Agrawal, T. K. Jha, B. Kumar, and S. K. Patra, *Phys. Rev. C* **98**, 035804 (2018), arXiv:1805.11963 [nucl-th].
- [20] Z. Carson, A. W. Steiner, and K. Yagi, *Phys. Rev. D* **99**, 043010 (2019), arXiv:1812.08910 [gr-qc].
- [21] N.-B. Zhang, B.-A. Li, and J. Xu, *Astrophys. J.* **859**, 90 (2018), arXiv:1801.06855 [nucl-th].
- [22] J. Margueron, R. Hoffmann Casali, and F. Gulminelli, *Phys. Rev. C* **97**, 025805 (2018), arXiv:1708.06894 [nucl-th].
- [23] Y. Yind and K. Kumamoto, *Phys. Rev. D* **98**, 023019 (2018).
- [24] Y. Fujimoto, K. Fukushima, and K. Murase, (2019), arXiv:1903.03400 [nucl-th].
- [25] J. Friedman, T. Hastie, and R. Tibshirani, *The elements of statistical learning*, Vol. 1 (Springer series in statistics New York, 2001).
- [26] B. Scholkopf and A. J. Smola, *Learning with kernels: support vector machines, regularization, optimization, and beyond* (MIT press, 2001).
- [27] I. Goodfellow, Y. Bengio, and A. Courville, *Deep learning* (MIT press, 2016).
- [28] R. J. Furnstahl, *Nucl. Phys. A* **706**, 85 (2002), arXiv:nucl-th/0112085 [nucl-th].
- [29] V. Baran, M. Colonna, V. Greco, and M. Di Toro, *Phys. Rept.* **410**, 335 (2005), arXiv:nucl-th/0412060 [nucl-th].
- [30] J. Margueron, R. Hoffmann Casali, and F. Gulminelli, *Phys. Rev. C* **97**, 025805 (2018), arXiv:1708.06894 [nucl-th].
- [31] J. Margueron, R. Hoffmann Casali, and F. Gulminelli, *Phys. Rev. C* **97**, 025806 (2018), arXiv:1708.06895 [nucl-th].
- [32] F. Douchin and P. Haensel, *Astron. Astrophys.* **380**, 151 (2001), arXiv:astro-ph/0111092 [astro-ph].
- [33] R. C. Tolman, *Phys. Rev.* **55**, 364 (1939).
- [34] J. R. Oppenheimer and G. M. Volkoff, *Phys. Rev.* **55**, 374 (1939).

- [35] F. Chollet, J. Allaire, *et al.*, “R interface to keras,” <https://github.com/rstudio/keras> (2017).
- [36] M. Abadi, A. Agarwal, P. Barham, E. Brevdo, Z. Chen, C. Citro, G. S. Corrado, A. Davis, J. Dean, M. Devin, S. Ghemawat, I. Goodfellow, A. Harp, G. Irving, M. Isard, Y. Jia, R. Jozefowicz, L. Kaiser, M. Kudlur, J. Levenberg, D. Mané, R. Monga, S. Moore, D. Murray, C. Olah, M. Schuster, J. Shlens, B. Steiner, I. Sutskever, K. Talwar, P. Tucker, V. Vanhoucke, V. Vasudevan, F. Viégas, O. Vinyals, P. Warden, M. Wattenberg, M. Wicke, Y. Yu, and X. Zheng, “TensorFlow: Large-scale machine learning on heterogeneous systems,” (2015), software available from tensorflow.org.
- [37] D. P. Kingma and J. Ba, “Adam: A method for stochastic optimization,” (2014), arXiv:1412.6980 [cs.LG].
- [38] C. Mondal, B. K. Agrawal, J. N. De, S. K. Samaddar, M. Centelles, and X. Viñas, Phys. Rev. **C96**, 021302 (2017), arXiv:1708.03846 [nucl-th].
- [39] Z. Carson, A. W. Steiner, and K. Yagi, Phys. Rev. **D100**, 023012 (2019), arXiv:1906.05978 [gr-qc].
- [40] H. Sotani, K. Iida, K. Oyamatsu, and A. Ohnishi, PTEP **2014**, 051E01 (2014), arXiv:1401.0161 [astro-ph.HE].
- [41] H. O. Silva, H. Sotani, and E. Berti, Mon. Not. Roy. Astron. Soc. **459**, 4378 (2016), arXiv:1601.03407 [astro-ph.HE].